

Supporting Information

Too Hot for Photon-Assisted Transport: Hot-Electrons Dominate Conductance Enhancement in Illuminated Single-Molecule Junctions

E-Dean Fung[†], Olgun Adak[‡], Giacomo Lovat[†], Diego Scarabelli[†], and Latha Venkataraman^{†‡}*

[†]Department of Applied Physics and Applied Mathematics, Columbia University, New York, NY 10027, U.S.A.

[‡]Department of Chemistry, Columbia University, New York, NY 10027, U.S.A.

Corresponding Author

*E-mail: lv2117@columbia.edu

Contents:

- S1 Experimental setup**
- S2 Additional data and error analysis**
- S3 Temperature dependent measurements**
- S4 Background Theory**
 - S4.1 Non-equilibrium electron distributions**
 - S4.2 Variations in plasmonic field enhancement**
 - S4.3 Full model under illumination**
- S5 Polarization dependence**
- S6 Enhancement in gold point-contacts**
- S7 Correlation between optical current and mechanical current**

S1 Experimental setup

The diagram of the home-build STM-BJ set-up with optical imaging capability is shown in Figure S1a. The bias voltage to the junction is applied using one of the analog voltage outputs of a National Instruments PXI-4461 data acquisition card. The current through the junction is fed into a transimpedance amplifier (Keithley 428 or Femto DLPCA-200) and the output from transimpedance amplifier is measured using an analog to digital converter input of NI PXI-4461. The piezoactuator used for controlling the electrode separation is driven with the second analog voltage output of NI PXI-4461, not shown, and the voltage across the junction is measured by the second input channel of the PXI-4461 card.

The optical microscope consists of an objective lens (Mitutoyo NIR x50), a beam splitter (Thorlabs BS029), a CCD camera, a laser diode, and a laser diode driver (Keithley 6221 or ILX Lightwave LDC-3722). The CCD camera is used for aligning the laser spot with the junction, as shown in Figure S1b. The laser diode is placed inside a Faraday cage in order to avoid electronic coupling to the circuit, while the entire setup is placed inside another Faraday cage to shield the junction from environmental noise.

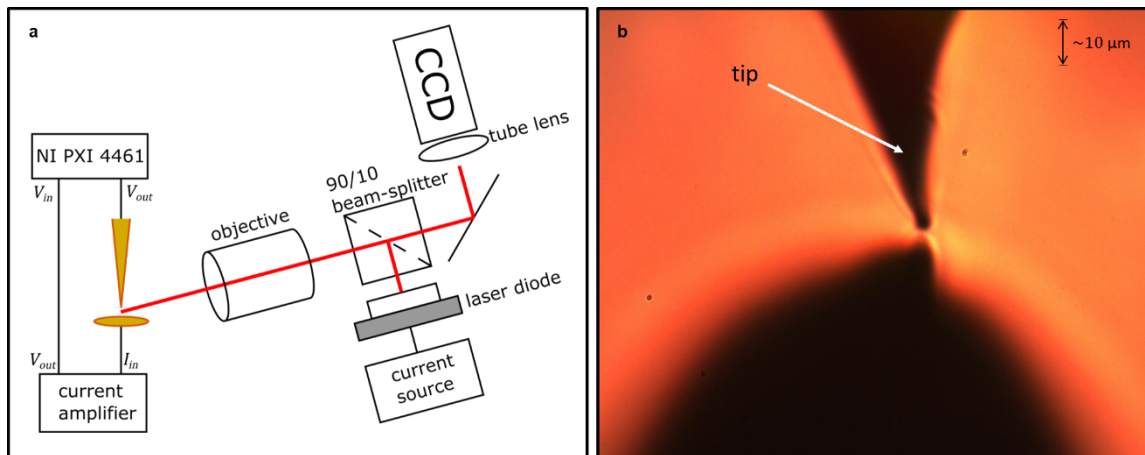


Figure S1. (a) Diagram of measurement set-up. (b) Optical image of tip used to produce data for Figure 1b in the main text.

S2 Additional data and error analysis

We performed experiments similar to the one discussed in the main text using BP samples that were not heated following molecule deposition. The high- and low-conducting peaks are both present. However, the high-conductance peak is significantly broader, likely due to the formation of junctions with two molecules in parallel. We see a clear enhancement under illumination in Figures S2a and S2b, demonstrating that the measurement is easily repeatable. These experiments were performed at 230 mV bias, and the enhancement in conductance extracted from the low-conductance peaks is around 60% for both experiments. Time dependence for Figure S2b is shown in Figure S2c. For Figure S2c, the high-conductance peak was extracted by fitting the high-conductance region (conductances above $2.5 \times 10^{-4} G_0$) to two Lorentzian peaks, taking the lower conducting peak to represent a single-molecule junction.

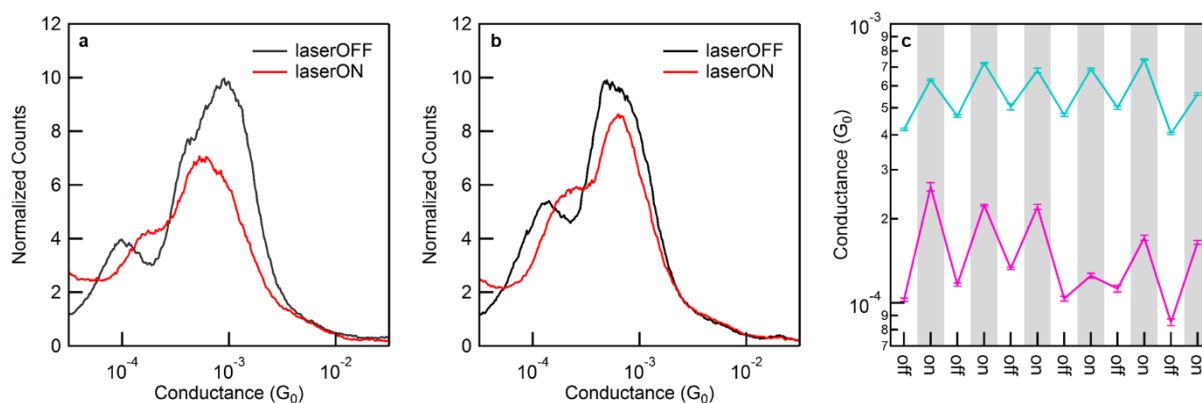


Figure S2. (a) and (b) show cumulative histograms for two additional experiments. (c) shows the extracted peak conductance values of (b) over time.

The standard error of the fitted peak values of the cumulative histograms, such as those found in Figures S2a,b and Figure 1b in the main text, is on the order of 2 milli-decades. This corresponds to a propagated standard error of 1% in the conductance enhancement.

As another measure of error, we break the experiment into four data sets: high conductance, laser off; low conductance, laser off; high conductance, laser on; and low conductance, laser on. Each data set is composed of N points, 1 point for each set of 500 traces. For example, in the case of Figure 1c in the main text, N is 9. The standard deviation of the conductance is 40 milli-decades for high-conductance peaks and 20 milli-decades for low-conductance peaks, regardless of whether the laser is on or off. This corresponds to a propagated standard deviation in the

conductance enhancement of 18% and 10% for high-conductance and low-conductance peaks, respectively. The propagated standard error is 6% and 3%, respectively. We note that both standard deviation and standard error are sensitive to sample size. Given the experimental constraints, it was impractical to collect more than 10 points in the manner described above. However, we did not find a single example where the low-conductance peaks show less enhancement under illumination than the high-conductance peaks. We provide the enhancement ratios of all experiments we performed where the high-conductance peak is sufficiently narrow in Table S1. For convenience, we report only the enhancement ratios calculated from the cumulative conductance histograms, though the enhancement ratios calculated by the other methods are similar as mentioned in the main text.

Table S1. Measured peak-conductance values and calculated on-off ratios

	high G, laser off (G_0)	low G, laser off (G_0)	high G, laser on (G_0)	low G, laser on (G_0)	on-off Ratio, high G	on-off Ratio, low G
1	5.63E-4	1.27E-4	7.16E-4	1.89E-4	1.27	1.33
2	5.86E-4	1.52E-4	7.60E-4	2.12E-4	1.29	1.39
3	5.52E-4	1.21E-4	7.17E-4	1.74E-4	1.29	1.44
4	6.29E-4	1.42E-4	6.87E-4	1.83E-4	1.09	1.29
5	5.53E-4	1.19E-4	6.12E-4	1.45E-4	1.11	1.22

S3 Temperature dependent measurements

The following data were acquired using the same STM-BJ method described in the main text. The only modification is the addition of a resistive heating element that increases the equilibrium temperature of the substrate. There is a thermoelectric current present since the tip and the substrate are not in thermal equilibrium with one another. However, as mentioned in the main article, the thermoelectric current is two orders of magnitude smaller than the bias-driven current.

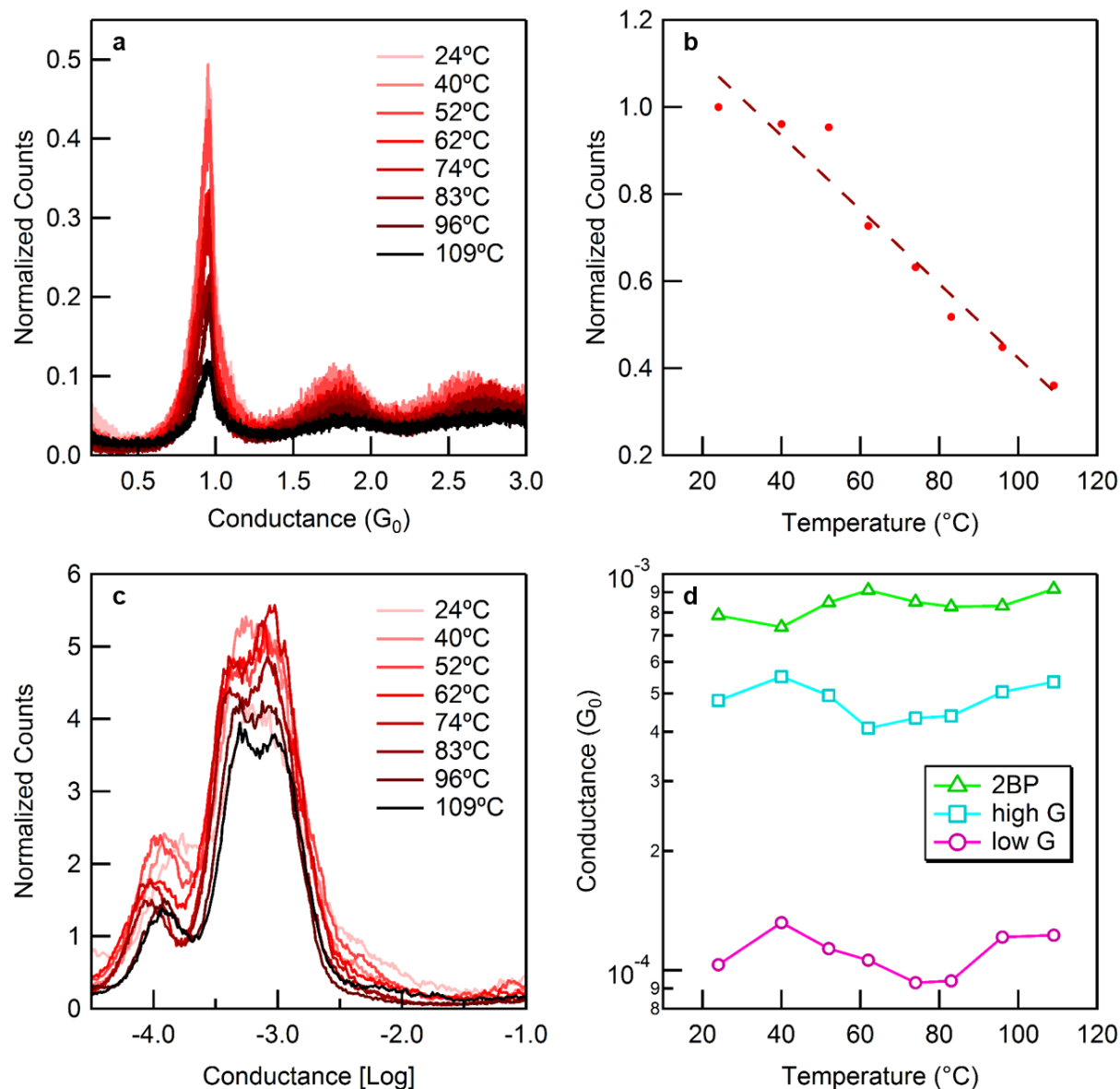


Figure S3. (a) Linearly-binned conductance histogram for atomic point-contacts measured in the presence of BP at a range of temperatures. (b) Number of points around $1 G_0$ peak normalized by the number of points at room temperature as a function of temperature. (c) Logarithmically-binned conductance histogram of the same data showing the molecular peaks at a range of temperatures. (d) Extracted peak conductance values as a function of temperature.

We collected data 2,000 traces at a time, increasing the temperature by approximately 10°C every time. Figure S3a displays the linearly-binned histogram, emphasizing the conductance for Au point-contacts. It is immediately clear that the number of points around the $1 G_0$ peak decreases monotonically with increasing temperature. We summed the number of points between

0.5 and 1.25 G_0 in the conductance histograms for each temperature and normalized by the number of points at room temperature to produce Figure S3b. The 1 G_0 pickup rate decreases linearly with increasing temperature, as described in the work of Huang and coworkers.¹ Using the fitted line, we estimate the temperature of junctions under illumination to be approximately 45°C.

Figure S3c presents the logarithmically-binned histogram, highlighting the conductance of BP. The double-molecule peak is particularly salient here. The most probable conductance in each peak is extracted for each temperature and plotted in Figure S3d. There is no clear increase in conductance with temperature, which implies that the enhancement in conductance observed under laser illumination cannot be explained by an increase in ambient temperature.

S4 Background Theory

S4.1 Non-equilibrium electron distributions

A number of theoretical explorations of transient non-equilibrium electron distributions have been made in recent years. We begin with the work of Govorov and coworkers.² The transient electron distribution is decomposed into two parts shown in Figure S4: a flat region from E_F to $E_F + \hbar\omega$ and a triangular region from E_F to $E_F + \hbar v_F q_n$, with complementary distributions below the Fermi energy for the hot-hole distributions. E_F and v_F are the Fermi energy and Fermi velocity, respectively, $\hbar\omega$ is the photon energy, and q_n is a wavevector for propagating plasmons. We neglect the triangular region since it is close to the Fermi energy; changes in the electron distribution in this area do not significantly impact the electron transport of BP because the transmission function for BP is nearly flat around the Fermi energy. We confirm this in section S4.3 of the Supplementary Information.

Turning to the work of Kornbluth et al.,³ we find an expression for the flat region between E_F to $E_F + \hbar\omega$.

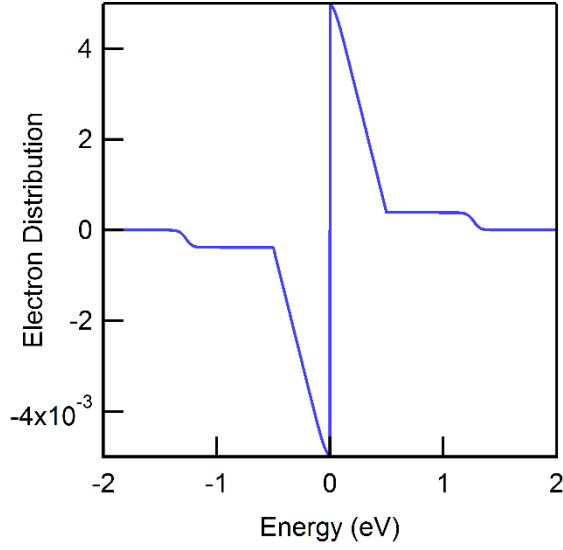


Figure S4. Electron distribution as described in reference [2].

$$f(E) = \Delta\rho_0 \tanh\left(\frac{E - E_F}{2k_B T}\right) \frac{\cosh\left(\frac{\hbar\omega}{k_B T}\right) - 1}{\cosh\left(\frac{\hbar\omega}{k_B T}\right) + \cosh\left(\frac{E - E_F}{k_B T}\right)} \quad (S1)$$

Equation 4 in the main text can be rewritten as

$$f_{hot}(E) = f'(E) + \Delta f(E)$$

$$\Delta f(E) = \Delta\rho_0 \tanh\left(\frac{E - E_F}{2k_B T}\right) \frac{\frac{1}{2}\left(e^{\frac{\hbar\omega}{k_B T}} - 1\right)}{\cosh\left(\frac{\hbar\omega}{k_B T}\right) + \cosh\left(\frac{E - E_F}{k_B T}\right)} \quad (S2)$$

In the limit that $\hbar\omega \gg k_B T$, eq. S1 can be closely approximated by eq. S2.

In order to estimate $\Delta\rho_0$, we make the following argument: Suppose that the field intensity is I . Then, the number of photons absorbed per unit volume, is:

$$n_{photon} = \frac{\alpha I}{\lambda \hbar \omega}$$

We estimate the absorption coefficient⁴ α using the complex index of refraction provided in the work of Olmon et al.,⁵ assuming the relevant length scale is given by λ . For $\hbar\omega = 1.27$ eV, α is approximately 38%. We take $\tau = 500$ fs and $\lambda = 30$ nm.⁶⁻⁹

Assuming that the absorption spectrum is flat (a reasonable assumption for Au near the Fermi energy), ΔQ_0 is simply given by

$$\Delta\rho_0 = \frac{n_{\text{photon}}}{g\hbar\omega} = \frac{\alpha\tau}{g\lambda(\hbar\omega)^2} \cdot I = \frac{\alpha\tau}{g\lambda(\hbar\omega)^2} \cdot \frac{c\epsilon_0}{2} |E|^2 = \frac{\alpha\tau c\epsilon_0}{2g\lambda e^2 d^2} \left(\frac{eV_{\text{opt}}}{\hbar\omega}\right)^2 \quad (\text{S3})$$

The density of states g is calculated assuming a free electron model.¹⁰ The value quoted in the main text takes $g = 1.6 \times 10^{22} \text{ eV}^{-1} \text{ cm}^{-3}$ and $d = 3 \text{ \AA}$.

S4.2 Variations in plasmonic field enhancement

There is an additional variable not discussed in the main text. Recent theoretical^{11–14} and experimental^{15–18} work have established that plasmonic enhancement can be damped by tunneling current. Since the two configurations of BP junctions have appreciably different tunneling current, it is possible that the increased enhancement observed in low-conducting geometries is due to additional field enhancement in the junction which in turn could give you an additional contribution to hot-electron population. We argue that because we used mechanically cut tips, the radius of curvature at the apex is relatively large, which results in a relatively small field enhancement. Since plasmonic field enhancement is small to begin with, we expect the effects of damping to also be small. This has been shown experimentally by Kravtsov and coworkers.¹⁹

S4.3 Full model under illumination

To show explicitly under what conditions PAT and hot-electron distributions are equivalent, we can write eq. 4 in the main text in the following form:

$$f_{\text{hot}}(E) = f'(E) + \Delta f(E)$$

$$\Delta f(E) = \Delta\rho_0 \left\{ f'(E - \hbar\omega) - 2f'(E) + f'(E) \frac{\cosh\left(\frac{E}{k_B T}\right) + e^{-\frac{\hbar\omega}{k_B T}}}{\cosh\left(\frac{E}{k_B T}\right) + \cosh\left(\frac{\hbar\omega}{k_B T}\right)} \right\} \quad (\text{S4})$$

Unlike in eq. S2, energy is referenced to the Fermi energy in eq. S4. One can prove that under most conditions ($|E| \gg k_B T$, $|E| \ll k_B T$, $\hbar\omega \gg k_B T$, $\hbar\omega \ll k_B T$), eq. S4 is closely approximated by

$$\Delta f(E) \approx \Delta\rho_0 \{ f'(E - \hbar\omega) - 2f'(E) + f'(E + \hbar\omega) \} \quad (\text{S5})$$

As illustrated in Figure 3a in the main text, this is precisely the effect of PAT. Figure S5a shows that even when $k_B T \sim E + \hbar\omega$, the qualitative behavior of eqs S4 and S5 is the same. Moreover, the effect of hot-electrons is larger when using eq. S4 instead of eq. S5. We do not anticipate any conditions where the steady-state behavior of PAT differs appreciably from that of hot-electron distributions.

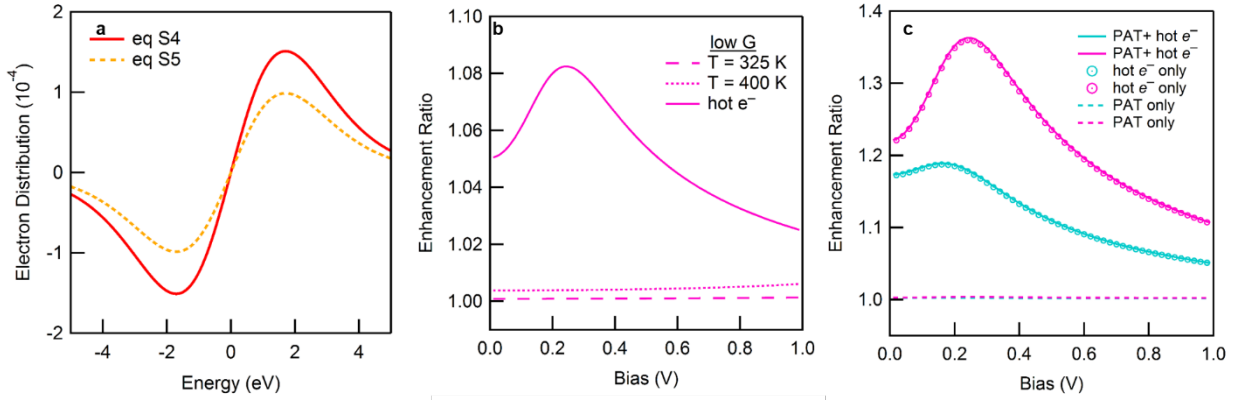


Figure S5. (a) The change in the electron distribution due to hot-electron generation as calculated from eqs S4 (solid curve) and S5 (dashed curve) for $k_B T = 1.2$ eV. (b) The calculated enhancement ratio as a function of bias assuming only Fermi-distributions at two temperatures (dashed curves). The solid line is the enhancement ratio assuming hot-electron distributions with no field enhancement at a temperature of 325 K. All calculations are performed using parameters for low-conducting junctions. (c) The enhancement ratio as a function of bias, with $V_{opt} = 4.5$ mV using full theory (solid line), only hot electron distributions (circular markers), and only PAT (dashed line). Teal curves are for high-conductance BP geometries and magenta curves are for low-conductance BP geometries.

Figures S5b reiterates that the conductance enhancement observed cannot be due to a change in the steady-state temperature at the junction. Even at temperatures where BP desorbs from the substrate, the expected conductance enhancement is less than 1%. Without assuming any field enhancement and only using hot-electron distributions, the conductance enhancement for the low-conducting configuration is still around 10 times larger than the enhancement possible with just equilibrium Fermi distributions.

Figure S5c shows that the majority of enhancement is due to hot-electron tunneling; the contribution of PAT to the enhancement is minimal. The V_{opt} required to achieve this enhancement is on the order of 4.5 mV, which corresponds to a field enhancement of 2.3 if we assume a local intensity of $5,770 \text{ kW}\cdot\text{cm}^{-2}$. This is likely an overestimate of the intensity. For more conservative estimates of the intensity, the field enhancement factor is on the order of 10.

To get a better sense of how the enhancement depends on the transmission function, we calculate the enhancement while varying the alignment parameter ε and the coupling parameter Γ , as shown in Figure S6a,b. The photon energy is fixed at 1.27 eV. As ε approaches the photon energy, the peak enhancement occurs at lower and lower bias. The value of the peak enhancement also increases dramatically. Decreasing Γ leaves the peak location the same but increases the enhancement ratio across all biases.

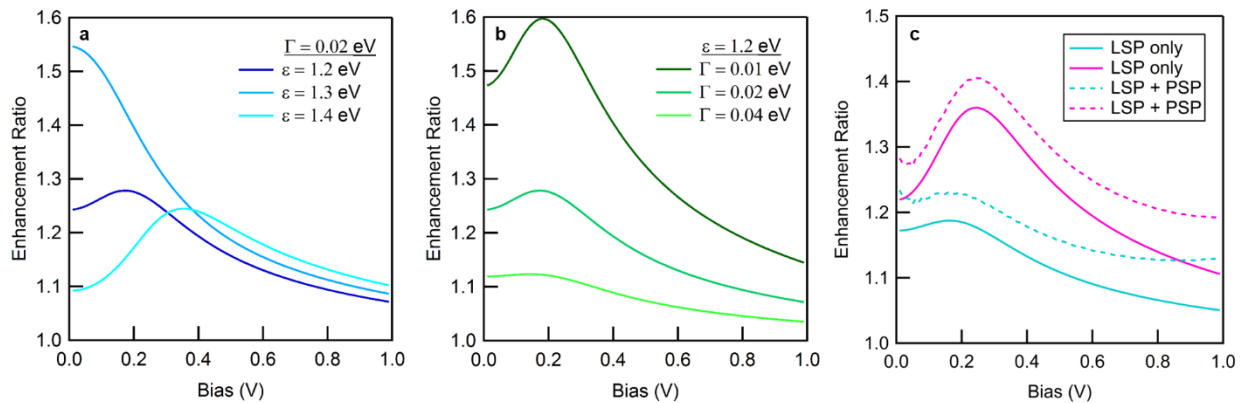


Figure S6: Enhancement ratio vs bias curves while varying (a) ε and (b) Γ . (c) Enhancement ratio vs bias curves assuming only localized surface plasmons (LSP) and including propagating surface plasmons (PSP). Teal curves correspond to high-conductance BP geometries, and magenta curves correspond to low-conductance BP geometries.

We show the effect of propagating surface plasmons (PSP) mentioned in Section S4.1 in Figure S6c. There is a 5% increase in enhancement across all biases, which is small compared to the effect of localized surface plasmons (LSP). In this calculation, we assumed a PSP energy of 0.5 eV and an amplitude of 0.1 (parameter A in eq. 5 of reference [2]).

S5 Polarization dependence

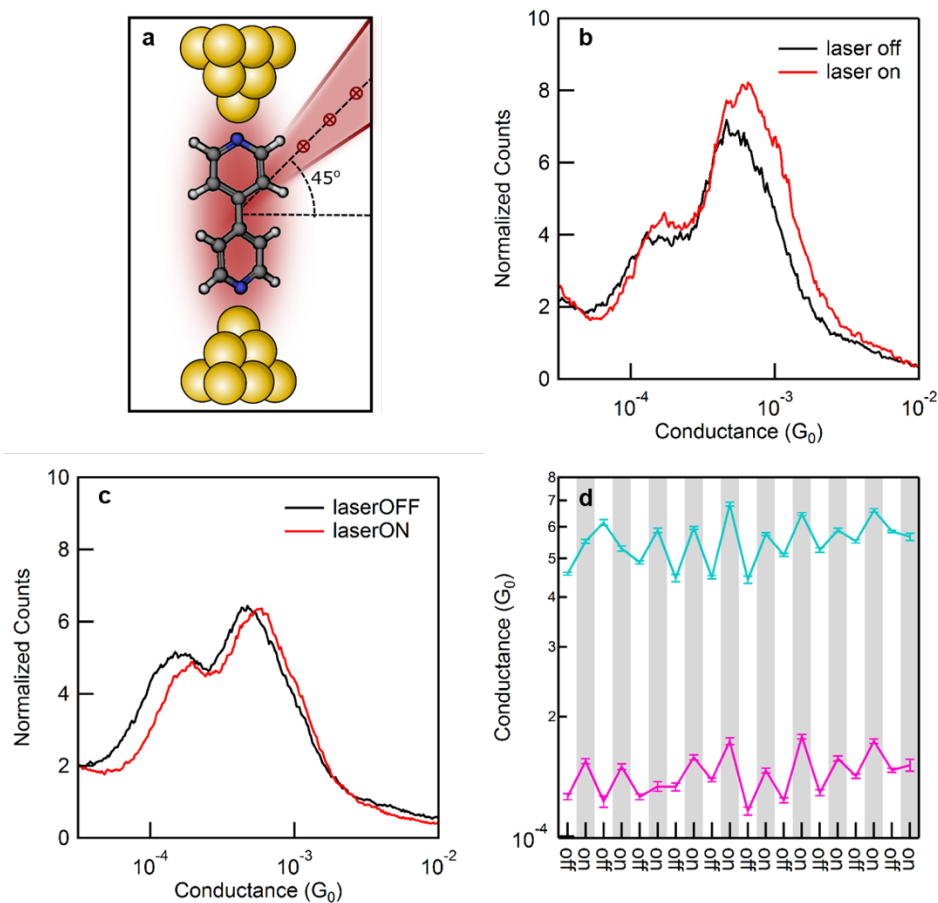


Figure S7. (a) Schematic of an illuminated metal-molecule-metal junction where polarization excludes PAT (direction of polarization is into/out of the plane). 1D conductance histograms of two independent experiments where the polarization excludes PAT performed at (b) 450 mV bias and (c) 300 mV bias. (d) shows the extracted peak conductance values of (c) over time.

We show in Figure S7 results from measurements made with the same laser but with the light polarization set to be perpendicular to the junction axis as shown in Figure S7a. We note that there is still a clear enhancement although the magnitude of this enhancement is smaller than what is observed with the field polarized along the junction axis. Table S2 summarizes the results from all experiments performed with the polarization perpendicular to the junction axis. The performance varies largely from experiment to experiment. Some experiments show no appreciable enhancement, whereas others show more enhancement than expected from calculations (see Figure S5b). We attribute this variability to inconsistent field enhancement in

the junction. We also note that propagating surface plasmons, which are not included in Figure S5b, may play a larger role at this polarization.

Table S2. Measured peak-conductance values and calculated on-off ratios for polarization perpendicular to junction axis

	high G, laser off (G_0)	low G, laser off (G_0)	high G, laser on (G_0)	low G, laser on (G_0)	on-off Ratio, high G	on-off Ratio, low G
1	5.58E-4	1.20E-4	1.20E-4	5.92E-4	1.06	1.04
2	5.57E-4	1.18E-4	1.18E-4	6.50E-4	1.17	1.20
3	4.96E-4	1.33E-4	1.33E-4	5.86E-4	1.18	1.14
4	6.30E-4	1.53E-4	1.53E-4	5.91E-4	0.94	1.01
5	6.31E-4	1.22E-4	1.22E-4	6.13E-4	0.97	1.00
6	4.83E-4	1.18E-4	1.18E-4	5.04E-4	1.04	1.06
7	5.25E-4	1.32E-4	1.32E-4	6.24E-4	1.19	1.22
8	5.32E-4	1.29E-4	1.29E-4	6.01E-4	1.13	1.23

S6 Enhancement in gold point-contacts

Previous experiments have demonstrated enhancement in electron transport in gold point-contacts.^{20,21} The transmission function is nearly anti-symmetric in the region 1.5 eV above and below the Fermi energy. Therefore, we expect the enhancement in the 1 G_0 peak to be small for the laser wavelength used here (980 nm = 1.27 eV). We are able to detect an enhancement on the order of 1% for some experiments. However, this is well within the experimental error. Higher photon energies and better defined tip geometries should improve the enhancement in gold point-contacts.

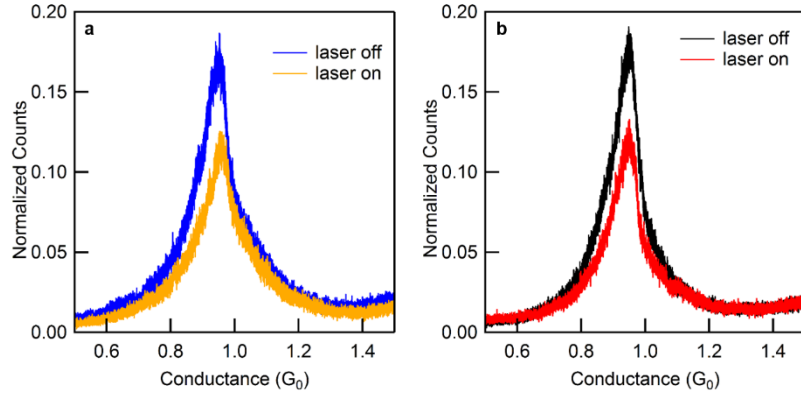


Figure S8. (a) Linearly-binned histogram of data from Figure 1b in the main text. (b) Linearly-binned histogram of data from Figure S2b demonstrating that the enhancement in the $1 G_0$ contact is not as robust as the enhancement in BP junctions.

S7 Correlation between optical current and mechanical current

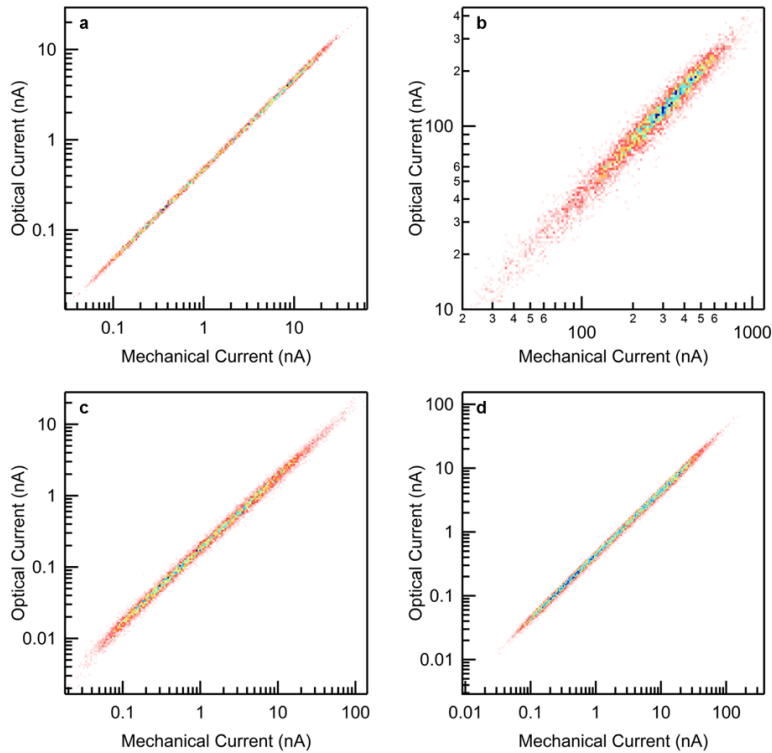


Figure S9. 2D optical current versus mechanical current histograms for (a) tunnel junctions and (b) gold point-contacts under 980 nm wavelength radiation. 2D optical current versus mechanical current histograms for tunnel junctions under (c) 405 nm and (d) 658 nm wavelength radiation.

References:

- (1) Huang, Z.; Chen, F.; D'agosta, R.; Bennett, P. A.; Di Ventra, M.; Tao, N. *Nat. Nanotechnol.* **2007**, *2*, 698–703.
- (2) Govorov, A. O.; Zhang, H.; Gun'ko, Y. K. *J. Phys. Chem. C* **2013**, *117*, 16616–16631.
- (3) Kornbluth, M.; Nitzan, A.; Seideman, T. *J. Chem. Phys.* **2013**, *138*, 174707.
- (4) Ziman, J. M. Optical Properties. *Principles of the theory of solids*; Cambridge University Press: Cambridge, 1999; pp 219-249.
- (5) Olmon, R. L.; Slovick, B.; Johnson, T. W.; Shelton, D.; Oh, S.-H.; Boreman, G. D.; Raschke, M. B. *Phys. Rev. B* **2012**, *86*, 235147.
- (6) Fann, W. S.; Storz, R.; Tom, H. W. K.; Bokor, J. *Phys. Rev. B* **1992**, *46*, 13592–13595.
- (7) Sun, C.-K.; Vallée, F.; Acioli, L. H.; Ippen, E. P.; Fujimoto, J. G. *Phys. Rev. B* **1994**, *50*, 15337–15348.
- (8) Sze, S. M.; Moll, J. L.; Sugano, T. *Solid-State Electron.* **1964**, *7*, 509–523.
- (9) Kanter, H. *Phys. Rev. B* **1970**, *1*, 522–536.
- (10) Ashcroft, N. W.; Mermin, N. D. The Sommerfeld Theory of Metals. *Solid state physics*; Saunders College Pub.: Fort Worth, 1976; pp 29-56.
- (11) Esteban, R.; Borisov, A. G.; Nordlander, P.; Aizpurua, J. *Nat. Commun.* **2012**, *3*, 825.
- (12) Esteban, R.; Zugarramurdi, A.; Zhang, P.; Nordlander, P.; García-Vidal, F. J.; Borisov, A. G.; Aizpurua, J. *Faraday Discuss.* **2015**, *178*, 151–183.
- (13) Zuloaga, J.; Prodan, E.; Nordlander, P. *Nano Lett.* **2009**, *9*, 887–891.
- (14) Zhu, W.; Esteban, R.; Borisov, A. G.; Baumberg, J. J.; Nordlander, P.; Lezec, H. J.; Aizpurua, J.; Crozier, K. B. *Nat. Commun.* **2016**, *7*, 11495.
- (15) Savage, K. J.; Hawkeye, M. M.; Esteban, R.; Borisov, A. G.; Aizpurua, J.; Baumberg, J. J. *Nature* **2012**, *491*, 574–577.
- (16) Mertens, J.; Eiden, A. L.; Sigle, D. O.; Huang, F.; Lombardo, A.; Sun, Z.; Sundaram, R. S.; Colli, A.; Tserkezis, C.; Aizpurua, J.; Milana, S.; Ferrari, A. C.; Baumberg, J. J. *Nano Lett.* **2013**, *13*, 5033–5038.
- (17) Ciraci, C.; Hill, R. T.; Mock, J. J.; Urzhumov, Y.; Fernández-Domínguez, A. I.; Maier, S. A.; Pendry, J. B.; Chilkoti, A.; Smith, D. R. *Science* **2012**, *337*, 1072–1074.
- (18) Tan, S. F.; Wu, L.; Yang, J. K. W.; Bai, P.; Bosman, M.; Nijhuis, C. A. *Science* **2014**, *343*, 1496–1499.
- (19) Kravtsov, V.; Berweger, S.; Atkin, J. M.; Raschke, M. B. *Nano Lett.* **2014**, *14*, 5270–5275.
- (20) Ittah, N.; Noy, G.; Yutsis, I.; Selzer, Y. *Nano Lett.* **2009**, *9*, 1615–1620.
- (21) Vadai, M.; Selzer, Y. *J. Phys. Chem. C* **2016**, *120*, 21063–21068.